G-Band FMCW Doppler Radar for Close-Range Environmental Sensing

Aleksanteri B. Vattulainen, *Graduate Student Member, IEEE*, Samiur Rahman, *Member, IEEE*, and Duncan A. Robertson, *Member, IEEE*

Abstract— Radar systems operating within the 220 GHz atmospheric transmission window are comparatively rare despite the benefits they offer in high angular, range, and Doppler resolutions. Given the growing availability of solid-state signal generation components designed for this frequency range, interest in the sensing potential of this region is increasing. This paper presents the development and characterization of 'Theseus', a 207 GHz FMCW Doppler radar designed for sea clutter and marine target characterization but also capable of a large variety of other close-range environmental sensing uses. The radar carrier frequency is tunable between 200-208 GHz with a maximum chirp bandwidth of 2 GHz resulting in a range resolution of 7.5 cm, and a chirp repetition interval (CRI) of 67.59 μs giving a maximum unambiguous velocity of ± 5.36 ms^{-1}. Several measurement application examples are presented, showcasing a wealth of micro-Doppler and micro-range information gathered from a variety of targets and clutter including sea clutter, humans swimming and running, UAV flight, a plan position indicator (PPI) scan of a terrestrial environment, and rain clutter. Data in this frequency band are very rare in the open literature, and thus the high range and Doppler resolution measurement capabilities of this radar present an opportunity to expand the knowledge in this area.

Index Terms— FMCW radar, Doppler radar, micro-Doppler, G-band, sub-THz, environmental sensing, sea clutter, target characterization.

I. INTRODUCTION

THERE is an emerging interest in radar operating in or near the 220 GHz atmospheric attenuation window wherein numerous potential applications have been identified, such as target detection, situational awareness, environmental sensing, meteorology, and security screening. This growing trend is driven by the increasing availability of signal generation technology for these frequencies, which had previously limited the feasibility of research in this area despite the great sensing potential.

The attraction of this atmospheric window is in the general advantages gained by higher carrier frequency radar, these being: finer angular resolution relative to antenna size,

smaller range cells by virtue of large bandwidths being feasible, and increased sensitivity to surface texture and to low Doppler velocities. These gains all produce a greater level of detail from the environment and targets within it. This paper presents a new frequency modulated continuous wave (FMCW) Doppler radar named 'Theseus' designed to make use of these advantages. The radar operates at a nominal center frequency of 207 GHz and is built from all solid-state components to produce a compact and low power-draw instrument designed for field deployment, where the combination of these features is a still a rarity.

A. Prior Art

Technologically speaking, components at this frequency use G-band or Y-band waveguide, defined as 140-220 GHz and 170-260 GHz respectively, both falling within the sub-THz region of 110-400 GHz. The technological challenges of working across the G-/Y-band range are broadly similar, so for the purposes of this discussion Y-band radars operating near the 220 GHz window are also included, though strictly speaking the Theseus radar is a G-band instrument.

To the authors' knowledge, the first system operating in the frequency range of interest mentioned in the literature dates from 1981 [1] with a follow-up paper of further measurement results of backscatter and attenuation of falling snow and rain at 140 and 225 GHz in 1988 [2]. The transmitter of this radar was a pulsed extended interaction oscillator, and further systems of this type were published starting in the late 1980s including: a dual polarized 140 GHz radar for general phenomenology studies [3], a 215 GHz radar used to measure backscatter from snow, trees, clouds and fog [4], [5], [6]; a 225 GHz polarimetric radar again measuring backscatter from trees and various natural surfaces [7], [8], [9]; and the first coherent radar at 225 GHz in 1991 used for the detection of targets and measurement of vehicle velocities [10]. These projects were carried out as fundamental phenomenological research into remote sensing, which was attractive in this frequency range given the advantages to resolution and antenna size stated previously, as well as a greater sensitivity to smaller hydrometeor particle sizes. This research was enabled by the advent of high-power vacuum tube sources but ultimately limited at the time by the cost, size, weight, power, cooling, and lifetime of these devices.

A scarcity of publishing then followed until a new 220 GHz system was presented in 2007, used for ISAR imaging and

concealed object detection. This is notable as the first example of G-band FMCW radar, and the first G-band radar based on solid-state components [11], [12], [13]. Further solid-state systems were then developed between 2008-2019 which were either of CW [14], FMCW [15], [16], [17], [18], [19], [20], [21], [22], [23], [24], [25], pulsed [26], or stepped-frequency configuration [27], [28], [29], [30], [31], [32]. Of these [28], [31], [32] are VNA based. These systems were used for various applications including the monitoring of vital signs, material characterization, imaging, security screening, and environmental backscatter studies. This renewed innovation was the result of an increasing availability of solid-state components, which allowed for FMCW operation and sources with higher bandwidths.

Further recent systems include: ViSAR, a high power pulsed travelling wave tube SAR system at 235 GHz which uses the shorter required aperture lengths at G-band to produce video-rate SAR imagery [33], [34]; a solid-state pulsed Doppler cloud-profiling radar at 199.5 GHz named GRaCE, where G-band provides better cloud penetration than lidar and greater sensitivity to particle size distribution than W-band and below [35] as well as a pulsed radar cloud-profiling satellite payload technology demonstrator at 238 GHz [36]; a differential absorption radar named VIPR operating around 170 GHz used for cloud humidity profiling from the ground and air, utilizing the presence of the 183 GHz water vapor absorption line for the sensing technique [37], [38], [39], [40]; and a mechanically scanned FMCW imaging radar at 223 GHz to research alternatives to lidar automotive sensing [41].

The review above represents the majority (if not all) of G-/Y-band systems present in the literature, to the authors' knowledge. The comparative rarity of these systems is due to the general challenges of working at these frequencies, where system components are expensive and relatively inefficient compared to W-band and below, and where the fundamental issues of low output power and high receiver noise figure are compounded by higher atmospheric absorption. Coherent systems with high chirp or pulse repetition frequencies, capable of measuring both range and significant Doppler velocities, are even rarer still [10], [19], [20], [26], [30], [33], [34], [35], [36]. The radar presented in this paper is not only Doppler capable, but has a fine range resolution, narrow antenna beam, and good phase noise performance which produces highly detailed measurements of targets and the environment. The instrument has also been designed to be field-deployable, resulting in a unique system with new measurement capabilities.

This paper then covers the design, development, characterization, and initial testing of a novel G-band FMCW Doppler radar. The radar is primarily designed for characterizing sea clutter and marine targets, where the motivation for this is outlined in Section II. Section III presents the resulting system design, Sections IV and V report the subsystem and system hardware results respectively, Section VI presents initial application measurements made with the radar, with the paper concluding in Section VII.

II. G-BAND MARINE RADAR DESIGN MOTIVATIONS

Autonomous surface vehicles (ASVs), have the potential to revolutionize the marine sector. Significant efficiency gains are possible by the removal or reduction of crew from often hazardous working conditions, where the space, energy, and design constraints imposed by life-support systems can be relaxed, and where mission times can be extended by the reduced needs for resupply [42], [43]. This benefits most vessel applications, including commercial shipping, defense, aquaculture, surveying, research, and the servicing of marine infrastructure.

We specifically consider sensing for small- to medium-sized ASVs where, compared to large ships, this class is more vulnerable to sea conditions and thus benefits from more detailed situational awareness. Due to their size, they are also potentially more agile than large ships and so are better able to act on alerts from instruments sensing their immediate environment. Currently, examples of ASVs in this class include AutoNaut [44], Saildrone [45], Sailbuoy [46], and C-Worker 5 [47], performing tasks such as surveying, research, and surveillance. The onboard navigational sensors can include GPS, electro-optical, automatic identification system (AIS) transceivers, and radar, depending on platform size. The sensing of these systems, although capable, limits them to either operating in daytime and clear weather, remote areas not requiring complex maneuvers or ship to ship interactions, or otherwise very low tonnage such that collisions are low risk.

Traditional marine radar systems usually fall somewhere in the S-, C-, or X-band [48], offering very long range (potentially tens of kilometers), all-weather and day/night active sensing. These sensors however have significant minimum ranges and are fundamentally unsuitable for high-detail situational awareness close to the vessel. Radar operating at a higher frequency, from mm-wave to sub-THz, could fill such a short-range sensing role. This would enable ASVs to navigate congested and complex environments such as harbors and coastal waters more reliably, where autonomy is challenging to provide.

For these reasons G-band radar is being investigated for this application and whilst limited to sensing at shorter ranges than conventional marine radar (due to propagation losses and signal generation technology), for small platforms this is not crucial given their inherent maneuverability. This has considerable parallels to terrestrial autonomy where E-band FMCW radar at 77 GHz has become a standard [49]. FMCW is preferred given the lower power consumption and greater system integration potential in solid-state designs. There is also a push towards sub-THz sensing in terrestrial autonomy [41], given the resolution gains, sensitivity to texture, and smaller sensor size [50]. These features are expected to be even more important for marine autonomy due to the greater sensing challenges caused by the dynamic environment, and coupled with advances in computation the additional information will enable emerging methods of target detection and classification.

The primary motivation for developing the radar in this paper is for the research of sea clutter phenomenology and
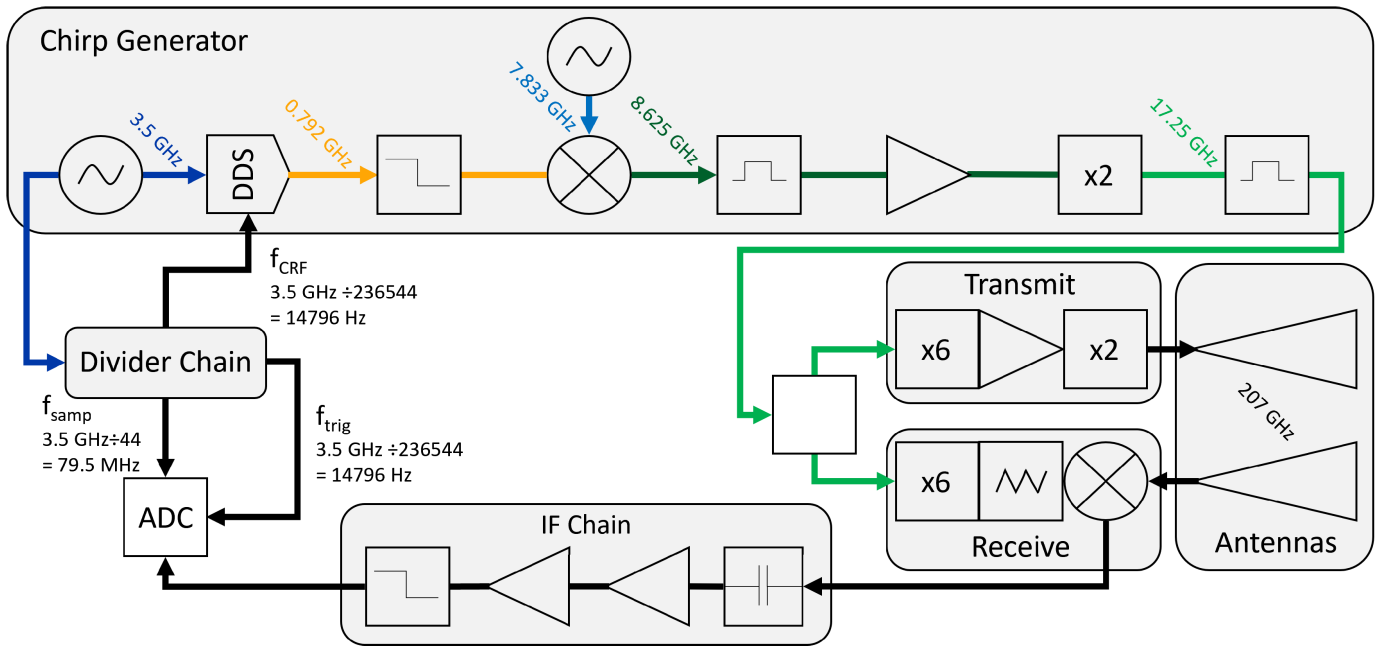
Fig. 1. Simplified system block diagram, where the indicated frequency outputs at each stage are for a final center frequency of 207 GHz.

the characterization of marine targets at G-band to pave the way for future radar design. Secondarily, this instrument is intended for general environmental sensing and target research as interest in radar at this frequency band grows. The production of this instrument was carried out as part of the STREAM project (Sub-THz Radar sensing of the Environment for future Autonomous Marine platforms) and is part of a measurement campaign using multiple radars with carrier frequencies in transmission windows within the range 24-300 GHz.

One of the project goals is the collection of empirical sea clutter data at low grazing angles, where sea clutter is caused by multiple scattering mechanisms and is described by observed amplitude and velocity distributions [51], [52]. Scattering is affected by both environmental conditions such as wave height, surface roughness, and wave direction, and by observation conditions including polarization, grazing angle, and radar frequency. Since wave direction and height can impact the chosen vessel bearing, sea clutter itself provides navigational information. It is also the background against which anomalies, including flotsam and jetsam, other vessels, marine mammals etc., are to be detected, where target signatures provide further information useful for detection, classification, and as an indication of possible behavior.

The most complete resource of empirical data on sea clutter backscatter is presently Nathanson's tables [53], however W-band results such as [54], [55], [56], and [57] are generally scarce. Additionally, this is only amplitude data, and Doppler data is less common still, although there has been some research up to W-band [58], [59]. At present, there is an outright absence of any such data at G-band, excepting the recent high grazing angle measurements with VIPR [40]. Those data are however not directly relevant to this research, as sensors onboard a surface platform observe at very low grazing angles, significantly altering the statistics.

During radar development, amplitude data at 94 GHz available from [56] was used as the closest indication of expected sea clutter normalized radar cross section (NRCS, σ^0). The justification and estimates of this and other system parameters are detailed in Vattulainen et al. [60] and further expanded on in the next section.

III. SYSTEM DESIGN

The work here presents the completed development of the radar system, where previously this was introduced in [60]. Notably, the system bandwidth has been reconfigured from 4 GHz to 2 GHz, the measured transmit power curve has been corrected, and the chirp generator redesigned to reduce phase noise.

A. System Architecture

The system block diagram is shown in Fig. 1. An FMCW design was chosen as is consistent with the motivation but also as a low power solid-state architecture which is suitable for field deployment. The signal generation scheme uses a direct digital synthesis (DDS) board to generate a linear frequency modulated (LFM) chirp centered at 792 MHz when operating at a final center frequency of 207 GHz. The chirp is then upconverted to an 8.625 GHz center against a dielectric resonator oscillator (DRO) signal at 7.833 GHz using the upper sideband. DDS chirp generation benefits from being highly linear and of low phase noise, preventing degradation of down-range scatterer point response and Doppler resolution. The system utilizes part of the design and components of a repurposed chirp generator [21] to then reach 17.25 GHz. The design specified in the previous publication [60] featured lower sideband conversion on a Micro Dynamics DRO-1000-05.56 model, 5.567 GHz DRO followed by a further doubling

stage, but these have since been replaced with a Nexyn NXOS-0783-01761 7.833 GHz DRO to improve phase noise performance. The results of this upgrade are detailed in Sections IV-C and V-B.

At 17.25 GHz, the chirp signal is split between the transmit and receive arms. Each uses a commercially available Quantum Microwave x6 multiplier to reach W-band. Given these multipliers accept ∼17 GHz as input, the DDS signal upconversion would ideally have been performed on a ∼16 GHz DRO to minimize increasing phase noise due to multiplication, however the availability of the existing Nexyn unit was the determining factor.

On transmit, the signal is amplified using a Spacek Labs power amplifier (PA), and the final x2 multiplication is achieved by a state-of-the-art Virginia Diodes Inc. (VDI) varactor doubler to reach G-band with a total multiplication factor of x24. The sourcing of PAs with an output power greater than +20 dBm at a frequency over 100 GHz within budget is the limiting factor on the transmit power and operating frequency for this radar. The measured output of the model used (published in [60]) begins to drop above 105 GHz making operation centered at the 220 GHz atmospheric window unfeasible. Varactor doublers are typically designed to accept up to 500-1000 mW of drive power, however they are still capable of high efficiencies at a lower drive power when correctly optimized. The unit in this design was optimized for a much lower drive level of ∼100 mW whilst still achieving ∼30% efficiency.

On receive, the output of the x6 multiplier serves as local oscillator (LO) for a Farran subharmonic mixer (SHM) used for homodyne down-conversion to intermediate frequency (IF) with the second harmonic. This design avoids the use of a second doubler for the LO, where the low LO drive level needed by an SHM is easily satisfied by the x6 multiplier.

Both the transmit and receive arms use identical Gaussian optics lens antennas (GOLAs) to provide high gain, low sidelobe beampatterns, with design details in Section III-B.

The IF chain consists of a DC block, two amplifiers, and a low-pass anti-aliasing filter which limits the ADC sampled signal to 0-32 MHz. The chirp repetition frequency f_{CRF} is derived from the DDS board 3.5 GHz clock DRO by a series of frequency dividers, and the ADC trigger frequency $f_{trig}=f_{CRF}$ is derived by further division to ensure coherent operation. Further details are provided in Vattulainen et al. [60].

Ideally, the radar would operate centered within the 220 GHz atmospheric window as this would minimize propagation losses, further to the main motivation of the STREAM project being to investigate the marine radar environment at as high a frequency as possible. As discussed above, the operating performance is limited to a band upper edge of 208 GHz by the performance of the W-band PA. Previously the band lower edge was imposed by spurious signals from the DDS when approaching its maximum operating frequency of 1400 MHz (which translated to the lower limit given the prior lower sideband mixing scheme). The new configuration removes this limitation giving access to lower frequencies, now limited by a bandpass filter lower edge at ∼8.3 GHz for a minimum transmit frequency of 200 GHz. This filter could be exchanged
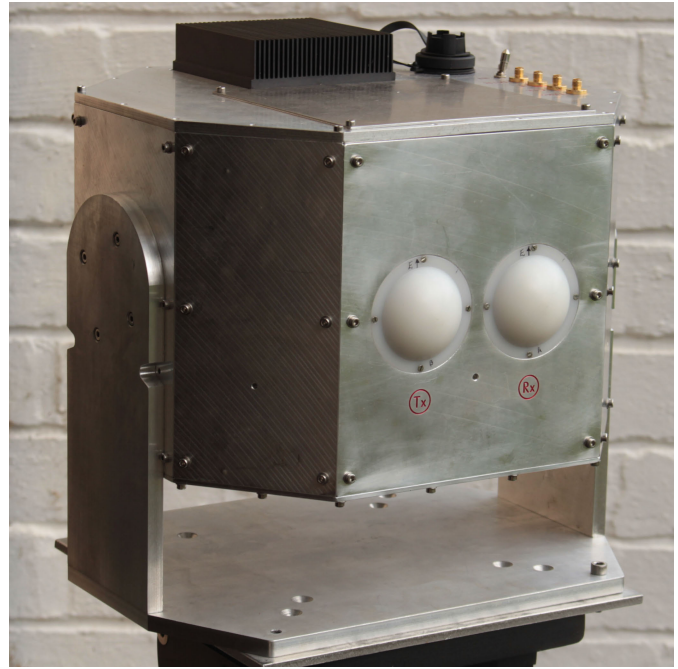

Fig. 2. The radar on a tripod, showing octagonal aluminum housing. The twin GOLAs are accessible from the top plate via a hatch, which allows change of polarization. Power and signal cables interface with the top plate.

later but given the rise in propagation losses towards the wings of the 183 GHz water line [61] this is not presently of interest for this project. Whilst this gives a total accessible chirp range of 8 GHz, for standard operation the chirp bandwidth is set to 2 GHz as this is deemed sufficient for sea clutter measurements whilst also maintaining Doppler resolution. For brevity, the ranges of 200-202 GHz and 206-208 GHz are termed low band and high band respectively. The antenna design is optimized for high band operation and thus there is a reduction in antenna gain of 0.44 dB (one-way) when operating at low band. In total, a gain in SNR of 2.46 dB is achieved from high to low band due to a greater transmit power and lower noise figure, as detailed in Fig. 9 in Section IV-D.

The mechanical design of the radar was driven by the need for a compact and waterproof enclosure able to fit into a 2-axis gimbal. The design was further constrained by the need to be relatively easy to manufacture from aluminum. This resulted in the design shown in Fig. 2, which uses numerous flat plates to reduce manufacturing complexity and allows better internal access for repairs or modifications, as opposed to an enclosure milled from a single solid piece [62]. The octagonal shape optimizes the interior space available whilst meeting the requirement for mounting in the curved yoke of a gimbal. The design also allows access to change the antenna polarizations by substitution of straight and twisted waveguide links, necessary since polarimetric diversity is a general requirement of clutter phenomenology measurements. Cooling is provided by a passive back-to-back heatsink assembly in the lid, visible in Fig. 2. The inner heatsink is forced air cooled to maximize thermal transfer from active components inside. Voltage regulators are mounted on the inner surface of the aluminum walls for further heat dissipation. The total DC power consumption
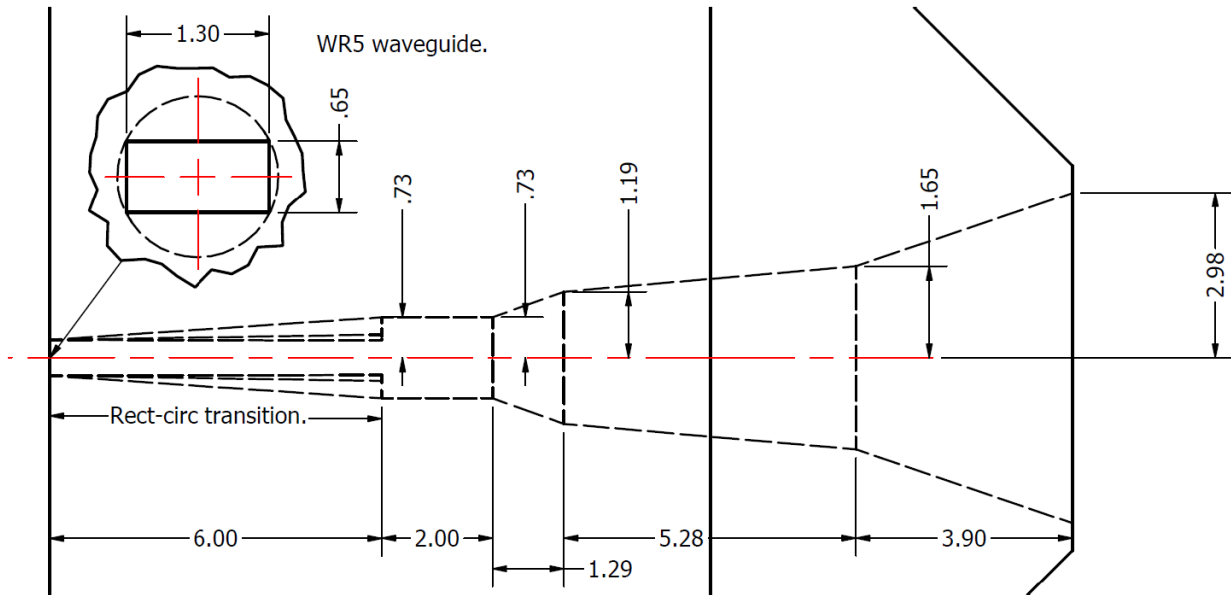
Fig. 3. The internal profile of the 207 GHz horn antenna with dimensions in millimeters.

of the instrument is 42.2 W, where this is dominated by the DDS ($\sim$10 W), x6 multipliers ($\sim$13 W together), and VDI doubler ($\sim$4 W). These values are the power dissipated in each component and its voltage regulator, where in the whole instrument 63% of power is dissipated in components and 37% in voltage regulators.

B. Antenna Design

The radar uses identical Gaussian optics lens antennas (GOLAs) on transmit and receive, yielding high transmit-receive isolation. This antenna type was chosen as it is both compact relative to a horn antenna of similar gain and could be manufactured in-house. The required gain of $\sim$39 dBi was determined by the link budget as outlined in [60], balanced with a need for practical beam footprint size and antenna pointing, yielding a one-way beamwidth of 2°.

The internal profile of the horn inside the GOLA design consists of several sections as shown in Fig. 3. The first of these is a WR-5 rectangular-to-circular transition followed by a short section of circular waveguide, after which the profile flares out with three conical sections of differing opening angle. This design is derived from a series of spline profiles published by Granet [63], each curve being approximated with a line for ease of manufacture.

The GOLA was designed using MATLAB, CORRUG and CST. For the horn, the beam waist, beam waist position, directivity, -3 dB beamwidth, Guassian coupling and optimized S11 at 207 GHz were 1.3 mm, 3.8 mm behind the aperture, 19.3 dBi, 19°, 98.7%, and -25.1 dB respectively. The horn was simulated as, and fabricated from, 65% Cu brass.

The lens was designed using equations from Goldsmith [64] for a spherical lens, produced from HDPE with a refractive index of 1.51 at 207 GHz (measured at the University of St Andrews). A lens with a diameter of 56 mm and a thickness of 18 mm was chosen as a compromise between edge taper,

lens thickness and total antenna length, where the simulated GOLA S11 was -32 dB at 207 GHz.

The simulated and measured horn patterns are shown in the following section in Fig. 4a along with the GOLA patterns in Fig. 4b and Fig. 4c, showing a good match to expected beam patterns and directivity in both cases.

IV. SUBSYSTEM CHARACTERIZATION RESULTS

A. Antennas

The principal plane antenna pattern at 207 GHz for unit A of the two GOLAs is shown in Fig.4b and Fig. 4c. The pattern for unit B was near identical. The mainlobe agreement with simulation is excellent down to -15 dB, and good down to below -45 dB. Notably there is a raised shoulder in both E and H, which is likely due to some small manufacturing error whereby the alignment of lens and horn is slightly off axis. A small spike seen at approximately $-18°$ in both H plane cuts is attributed to multipath effects. The beamwidth values deviate from simulation by 0.1° in E and 0.06° in H for unit A, and 0.12° and 0.06° for unit B. The achieved low sidelobe level of <-35 dB is desirable for the instrument application since off-axis scatterers may increase the reflected transmitter phase noise thereby reducing instrument sensitivity, hindering measurements of the lower end of the amplitude distribution of low NRCS sea clutter and subsequently inflating NRCS estimates. Low sidelobes also minimize artifacts in PPI scans.

Antenna gain for each unit was measured by gain substitution with a G-band standard gain horn. This yielded measured values of 38.1 dBi for unit A and 38.1 dBi for unit B, whilst the simulated gain was 38.9 dBi. Some of the discrepancy is attributed to uncertainty in the complex permittivity of HDPE at 207 GHz. The full S11 results for the antenna are published in [60], where the measurements revealed a resonance pattern with an S11 of <-20 dB over the 2 GHz bandwidth centered at 207 GHz. Measured and simulated gain values are presented
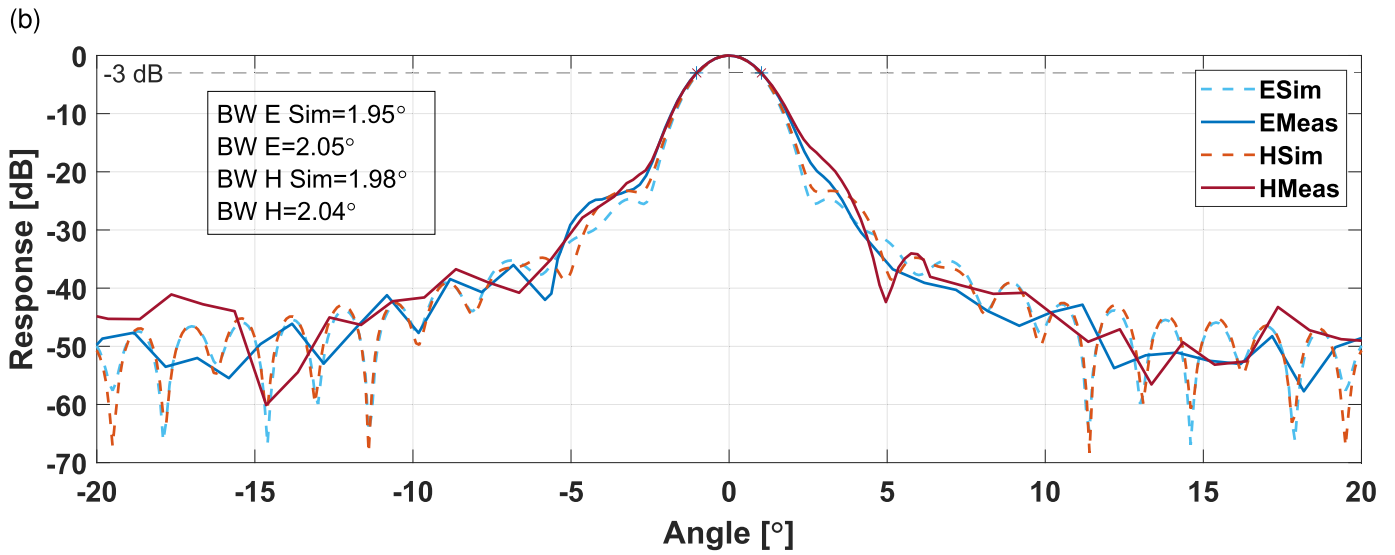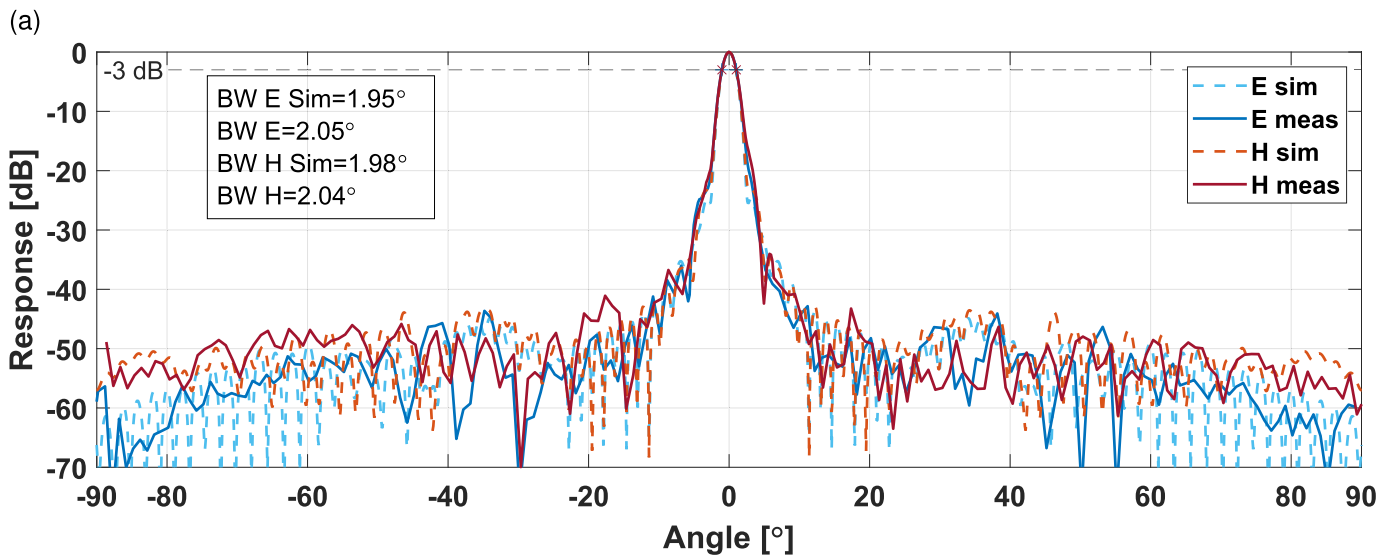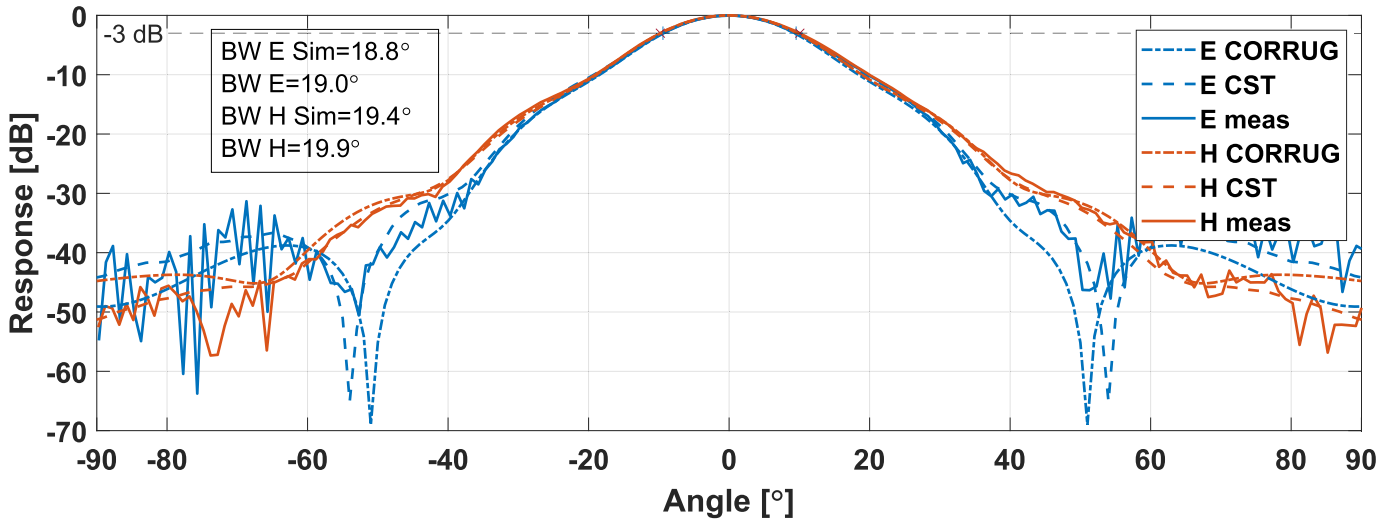
Fig. 4. (a) The antenna pattern of horn unit A at 207 GHz, which is also representative of unit B. For comparison, the CST and CORRUG simulations are overlaid. (b) The GOLA antenna pattern at 207 GHz for unit A which is also representative of unit B, (c) detail of the mainlobe with a beamwidth of approximately 2°, both with CST simulations overlaid.

TABLE I

SIMULATED AND MEASURED VALUES FOR GOLA UNIT A BEAMWIDTHS IN E AND H PLANES, DIRECTIVITY D, GAIN G, AND LOSS L. THE SUBSCRIPTS m AND s INDICATE MEASURED AND SIMULATED VALUES RESPECTIVELY. THE MEASURED RESULTS FOR UNIT B WERE VERY SIMILAR

f (GHz)	E_{sim}(°)	E_{meas}(°)	H_{sim}(°)	H_{meas}(°)	D_{sim} (dBi)	G_{sim} (dBi)	G_{meas} (dBi)	L (dB)
200	2.00	2.12	2.06	2.17	38.98	38.50	37.43	1.55
207	1.95	2.05	1.98	2.04	39.35	38.87	37.87	1.48
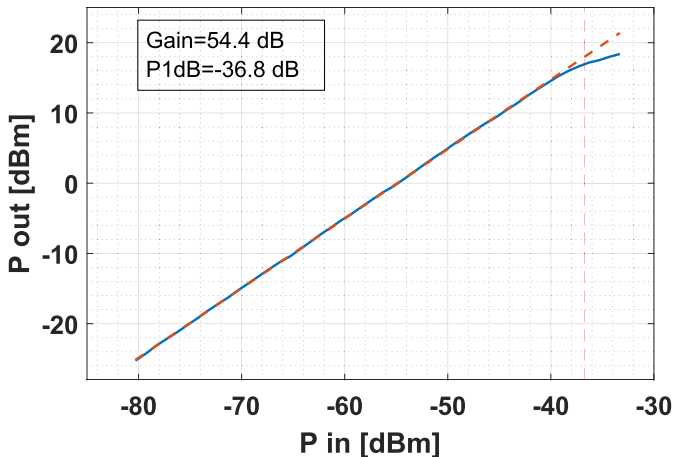
Fig. 5. IF chain compression curve for an input signal of 10 MHz.

Fig. 6. IF gain versus frequency at an input level of −50 dBm.

at 200 and 207 GHz (low and high band) in Table I, where the measured gain values include an additional 0.25 dB loss due to the waveguide links. The value for antenna loss is calculated as the difference between the simulated directivity (from CST) and the measured gain.

B. IF Chain

As shown in Fig. 1, the IF chain consists of: Mini Circuits BLK-18 DC block, Wenteq Microwave Corp. ABL0050-00-3310 low noise amplifier, Mini Circuits ZFL-500HLN, and Mini Circuits SLP-30 lowpass filter. Fig. 5 shows the compression curve of the IF chain for a 10 MHz input frequency. The gain for the linear region is 54.4 dB, reaching the −1 dB compression point at −36.8 dBm, for a maximum undistorted output level of +16.6 dBm. In practice the dynamic range upper bound of the radar is limited to +10 dBm by the maximum allowable input signal to the ADC. The amplifiers are arranged in order so that the Wenteq model is first as it has high gain with low noise, and so minimizes the receiver noise figure. The Mini Circuits amplifier is second due to its higher −1 dB compression point, preventing signal compression occurring before reaching the maximum input signal of the ADC. The previous iteration of the IF chain featured a different second amplifier which caused excessive harmonic distortion in the receiver. This was exchanged for the current model which has a better −1 dB compression point, where the difference can be seen in Fig. 12, where the new configuration data comes from measurements with the current second IF amplifier.

Fig. 6 shows the IF gain versus frequency, where a rise at low frequency quickly decays to a region between 5-32 MHz where the level drops nearly linearly by ∼2 dB, mainly due

to the second amplifier. A steep gain roll-off then occurs after 32 MHz due to the anti-aliasing SLP-30 (nominally 30 MHz cut-off frequency). The low frequency cut-off behaviour is dominated by the DC-block. Ideally the gain curve would be flat prior to the anti-aliasing filter roll-off as this prevents an additional range dependent amplitude variation in the received signal, for example in range-time-intensity (RTI) plots. The drop of 2 dB represents only a minor departure from this however, and does not impair the interpretability of results. For measurements of clutter or target backscatter, this variation is accounted for by the range calibration. In general, the sensitivity of the radar is unchanged as the gain affects signal and noise equally, and the variation is low enough to consistently maintain signal within the dynamic range of the ADC.

C. Chirp Generator

Fig. 7 presents the chirp generator output power as a function of frequency, which on average is +5.2 dBm and flat to within ±0.3 dB in the low and high bands as indicated, each being 167 MHz in bandwidth (translating to an output bandwidth of 2 GHz). A measurement of DDS spectra across the operational range in frequencies of 500.333-833.667 MHz revealed no spurs which could negatively impact performance.

Fig. 8 shows the results of a phase noise measurement for the previous [60] and current chirp generator configurations. The measurement was performed with an HP 4352B phase noise analyzer by down-converting the 17 GHz signal against a low phase noise reference oscillator at 13.6 GHz. The previous configuration featured a Micro Dynamics DRO at 5.567 GHz which was exchanged for a Nexyn unit at 7.833 GHz with
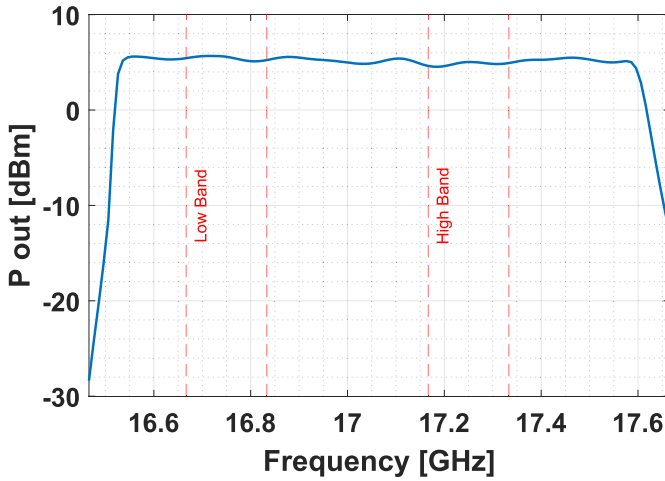
Fig. 7.   Chirp generator output power versus frequency, indicating the range of low and high band operation.
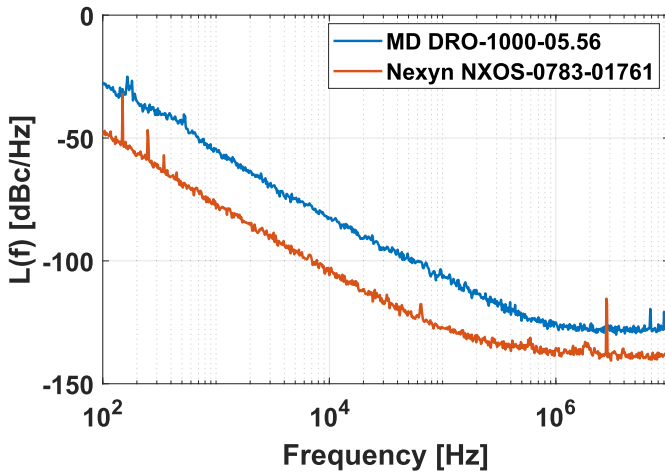

Fig. 8.   Chirp generator phase noise for an output frequency of 17 GHz for old (MD DRO-1000-05.56) and new (Nexyn NXOS-0783-01761) configurations.

the removal of a doubling stage, as stated in Section III-A. Fig. 8 shows an averaged improvement of 21.5 dB over offset frequencies from 100 Hz to 100 kHz at a 17 GHz output, attributed to better intrinsic phase noise performance from the Nexyn DRO and to a $20\log_{10}(2)=6$ dB reduction due to the removal of a doubling stage given the higher oscillator frequency and change from lower to upper sideband upconversion.

D. Transmit Power and Noise Figure

The noise figure of the receiver is shown in Fig. 9, produced using three runs of Y-factor measurements. The Y-factor measurements were carried out by measuring the integrated IF power at a given DDS frequency whilst the antenna was first pointed at room temperature (293 K) radio frequency absorber, and then comparing this to a similar run of measurements taken whilst pointing the antenna at absorber immersed in liquid nitrogen (77 K). The Y-factor measures the full double sideband (DSB) noise of the receiver. These measurements showed good agreement and were averaged for the plot shown. The band average noise figure of the system is 12.1 dB for
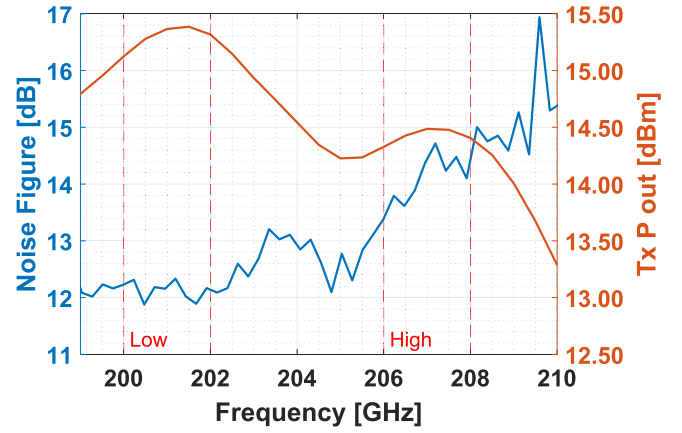

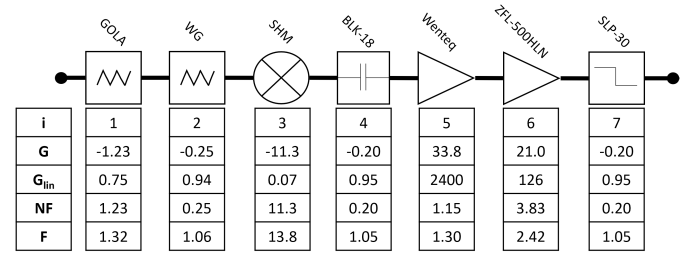Fig. 9.   Receiver noise figure and transmit power.

Fig. 10.   Receiver block diagram, listing the position (i), gain [dB] (G), linear gain (G_{lin}), noise figure (NF) and noise factor (F) of each component. The GOLA, waveguide, and SHM performance values were averaged over high band and a frequency of 10 MHz was assumed for the IF chain.

low band (200-202 GHz), rising to 14.1 dB for high band (206-208 GHz).

The Friis formula for noise factor is shown in Eq. 1:

$$F_{\text{t}} = F_1 + \sum_{i=2}^{Q} \left(\frac{F_i - 1}{\prod_{j=1}^{i-1} G_{\text{lin},j}} \right) \tag{1}$$

where F_t is the total noise factor of the receiver, Q is the total number of components in the chain, and F_i and $G_{\text{lin},j}$ are the noise factor and linear gain value of a component in the cascade as shown in Fig. 10, along with the decibel gain G and noise figure NF. Eq. 1 was used to infer the mixer conversion loss L_{c} and noise figure NF_{mix} in each band from the receiver noise figure values, however since no direct measurement of the conversion loss is made and the exact relationship between L_{c} and NF_{mix} is unknown then it is assumed that $NF_{\text{mix}} = |L_{\text{c}}|$. In general, the SHM L_{c} varies since in this design the LO drive level is not optimized at each frequency, given this is difficult to achieve for chirped operation. Using this method, the SHM L_{c} is estimated to be 9.2 dB and 11.3 dB in low and high band respectively. The total receiver gain (defined from the RF port of the SHM) is then calculated to be 45.2 dB at low band and 43.1 dB at high band.

Table II provides a summary of the subsystem results for the radar, including the average transmit power from the doubler output port, this being $+15.3$ dBm for low band and $+14.4$ dBm for high band, as read from Fig. 9.

TABLE II
MEASURED AND DEFINED RADAR PARAMETERS

| Parameter	Low band	High band
Transmit power	+15.3 dBm	+14.4 dBm
Receiver noise figure	12.1 dB	14.1 dB
Antenna gain	37.43 dBi (mean)	37.87 dBi (mean)
Antenna -3 dB beamwidth	2.13° (mean)	2.05° (mean)
Bandwidth/range resolution	2 GHz/7.5 cm	2 GHz/7.5 cm
Polarization	HH, VV, HV, VH	HH, VV, HV, VH
CRF/CRI	14.796 kHz/67.59 μs	14.796 kHz/67.59 μs
Chirp duration	51.49 μs	51.49 μs
Sampling rate	79.55 MHz	79.55 MHz
Maximum unambiguous velocity	± 5.36 m s^{-1}	± 5.36 m s^{-1}
Maximum unambiguous range	153.5 m	153.5 m
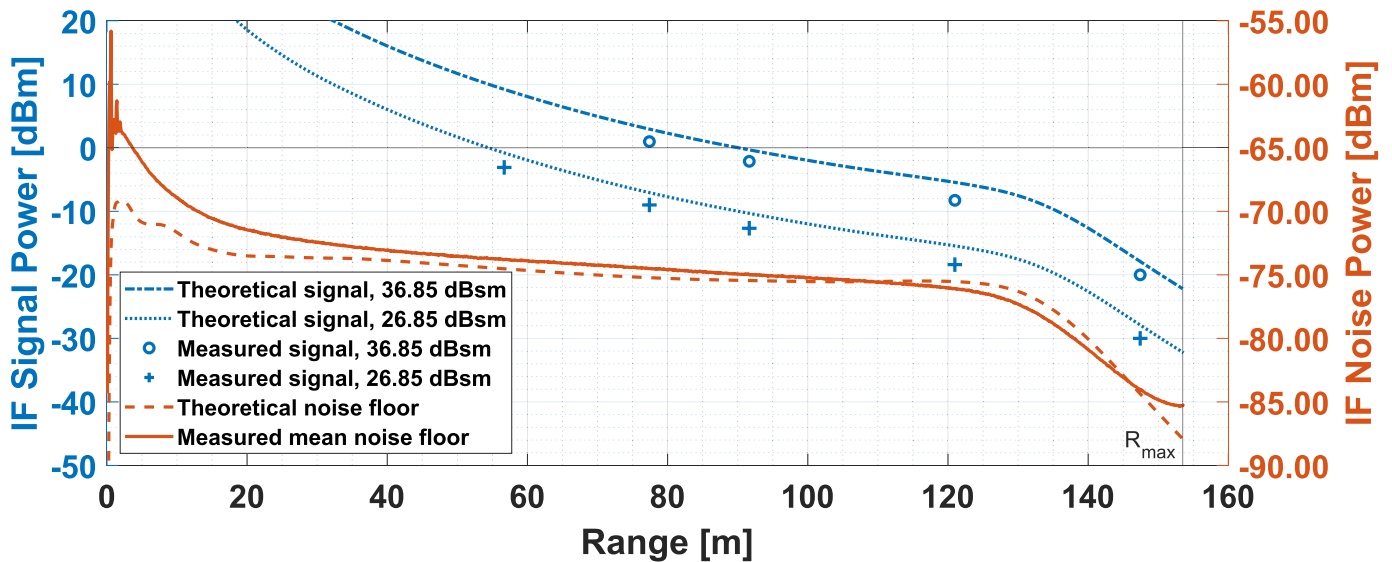
Fig. 11. Measured radar range calibration results compared with simulated curves produced using values measured from the characterization of the radar, presented in Table II. System predicted and measured noise floor curves (sky-point data) are also displayed. The measured mean noise floor plateau level is ~ -74 dBm for a bin width of 19.4 kHz, decreasing slightly with increasing IF frequency before following the roll-off of the IF chain low-pass filter.

V. SYSTEM CHARACTERIZATION RESULTS

A. Range Calibration and System Noise Floor

The range calibration curves shown in Fig. 11 were generated using the results for the subsystem measurements, shown in Table II, the measured IF gain shown in Fig. 6, and accounted for the atmospheric loss during the measurement using the 'gaspl' function of MATLAB, based on the 2013 ITU model for atmospheric attenuation [61]. The recorded atmospheric conditions at the closest weather station (Leuchars, 5.3 km from the measurement site) were a pressure of 100800 Pa, temperature of 18.5 °C, and a relative humidity of 59.7% = 9.44 g m^{-3}, which results in a two-way path loss of 0.72 dB at 100 m. Measurements were made to find the averaged signal level from two precision trihedrals at a selection of ranges. The RCS values of the triangular trihedrals were calculated to be 26.85 dBsm and 36.85 dBsm (side length 124 mm and 223 mm respectively) for a center frequency of 207 GHz, for measurements made with flattop

windowing. The average difference between the measured points and simulated curves was -1.61 dB. This indicates that the characterization results presented have good accuracy, and where the remaining averaged loss will be accounted for in future calibrated measurements. The general trend of the points and the curves also matches well and so the system hardware is behaving as expected as a function of range.

The measured mean system noise floor (recorded by a sky-pointing measurement) is also shown in Fig. 11, where this generally fits the expected profile very well and only slightly deviates at close range (within 20 m). This region corresponds to ≤ 5 MHz, which would indicate this rise is due to increased $1/f$ noise from the SHM at low IF frequencies, however this will not impair measurement capabilities given that at this range ample SNR will be provided by greater link-gain. The noise floor is gently sloping due to the frequency response of the IF chain shown in Fig. 6, with a plateau level of ~ -74 dBm. The measured noise floor is range processed using a -92 dB Four-Term Blackman-Harris window which
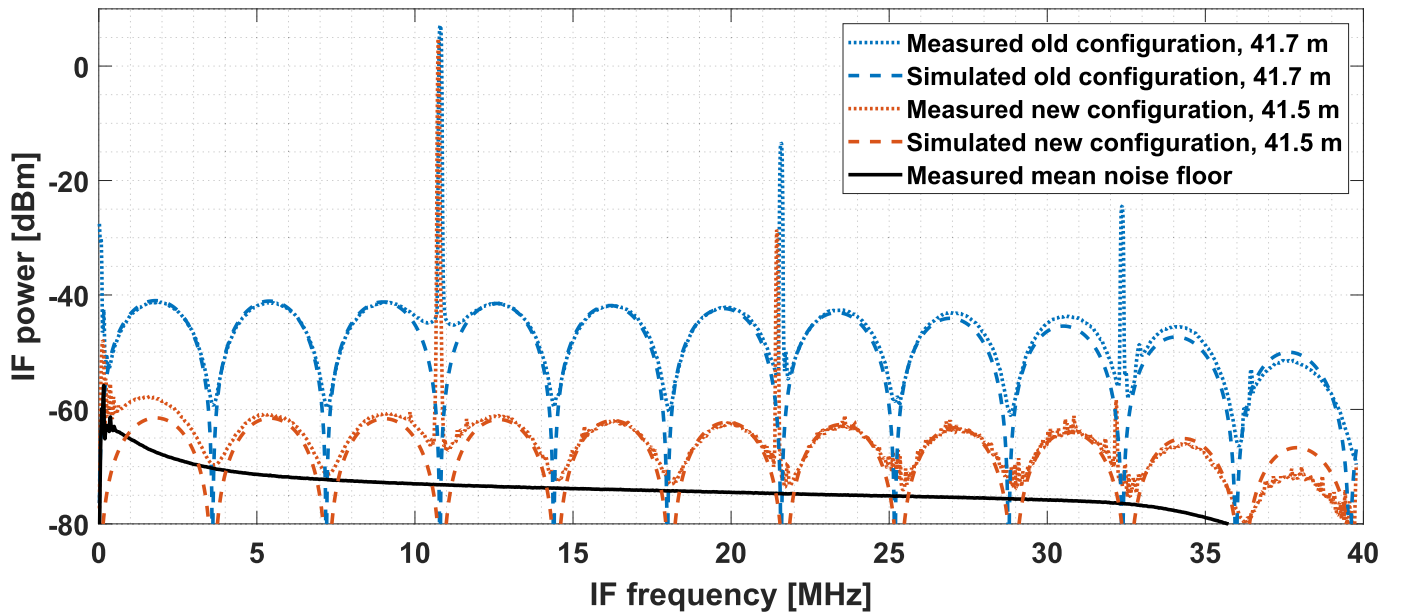
Fig. 12. Measured trihedral range profiles and simulated noise floors for both old and new chirp generator configurations. The phase noise cancellation effect causes a lobed pattern to appear when observing a bright target, where the period of the lobes is related to the target range as shown by Eq. 3, with this being used in Eq. 4 to plot the simulated noise floors. The prominence of the effect depends on the degree of system phase noise, and this is significantly reduced with the new configuration.

increases the noise bandwidth by a factor of 2.0045 [65], however the associated gain is also removed during range processing. The mean level of the whole curve is -74.7 dBm, which is very close to the average theoretical value of -75.5 dBm per FFT bin as predicted by the noise factor results from Y-factor measurements detailed in Section IV-D. This shows good agreement between both measurements of system noise.

The noise floor has a slope of ~ 4.5 dB from -71.5 dBm at 20 m (5.2 MHz) to -76.0 dBm at 120 m (31.1 MHz). Beyond this the noise floor roll-off begins due to the IF anti-aliasing filter. The range-frequency relationship is shown in Eq. 2:

$$R = \frac{f c t_c}{2B} = 3.859 \times 10^{-6} [\mathrm{m\,s}] \cdot f[\mathrm{Hz}] \qquad (2)$$

where t_c is the chirp time and B is the chirp bandwidth. As the plateau noise floor level is ~ -74 dBm and the maximum input signal to the ADC is $+10$ dBm, the dynamic range of the radar is 84 dB.

B. Noise Floor Degradation From Phase Noise

Transmitter phase noise in FMCW radars can contribute to the noise floor of the instrument when reflected from bright targets or clutter. The effect causes a lobed pattern (on a decibel amplitude scale) with a period depending on the target range. This modulation, M, is known as phase noise cancellation and is shown in Eq. 3:

$$M = 4 \sin^2\left(2\pi \frac{R}{c} f\right) \qquad (3)$$

where R is the target range and f is the IF frequency of a given range bin, and relates to the frequency offset from the carrier in the phase noise measurement shown in Fig. 8. Due to this effect, extended targets and distributed clutter can cause a general increase (without distinct modulation) in the radar
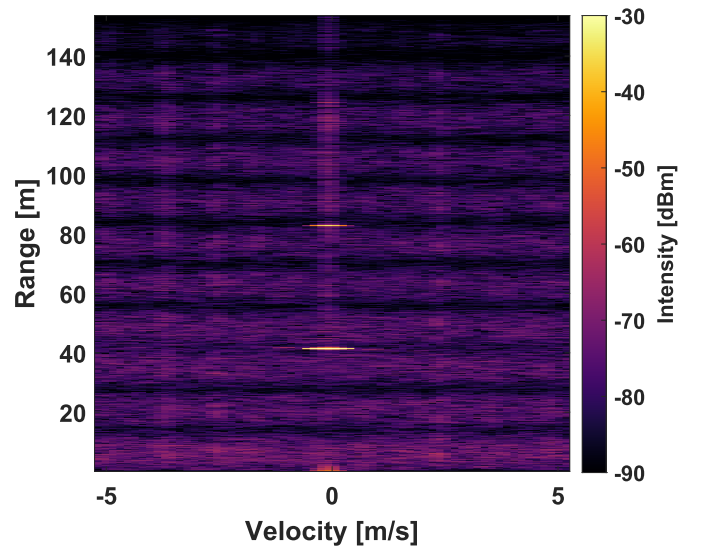

Fig. 13. Range-Doppler plot (processed with a CPI of 512 chirps) for the old configuration illustrating the phase noise cancellation effect caused by a bright target (trihedral), and the banding pattern this produces in the noise floor which will obscure weak targets across all Doppler bins at the affected ranges.

noise floor if phase noise is not adequately controlled [66]. This effect was noted in the performance of the radar with the previous chirp generator configuration. This was the primary reason for its modification, since the effect reduced the ability of the radar to observe low level clutter in general, and particularly affected measurements of clutter in the presence of bright targets.

Fig. 12 shows range profiles measured using a trihedral target at approximately the same range for both the old and new chirp generator configurations. In each measurement, the target was rotated off boresight such that the signal level was
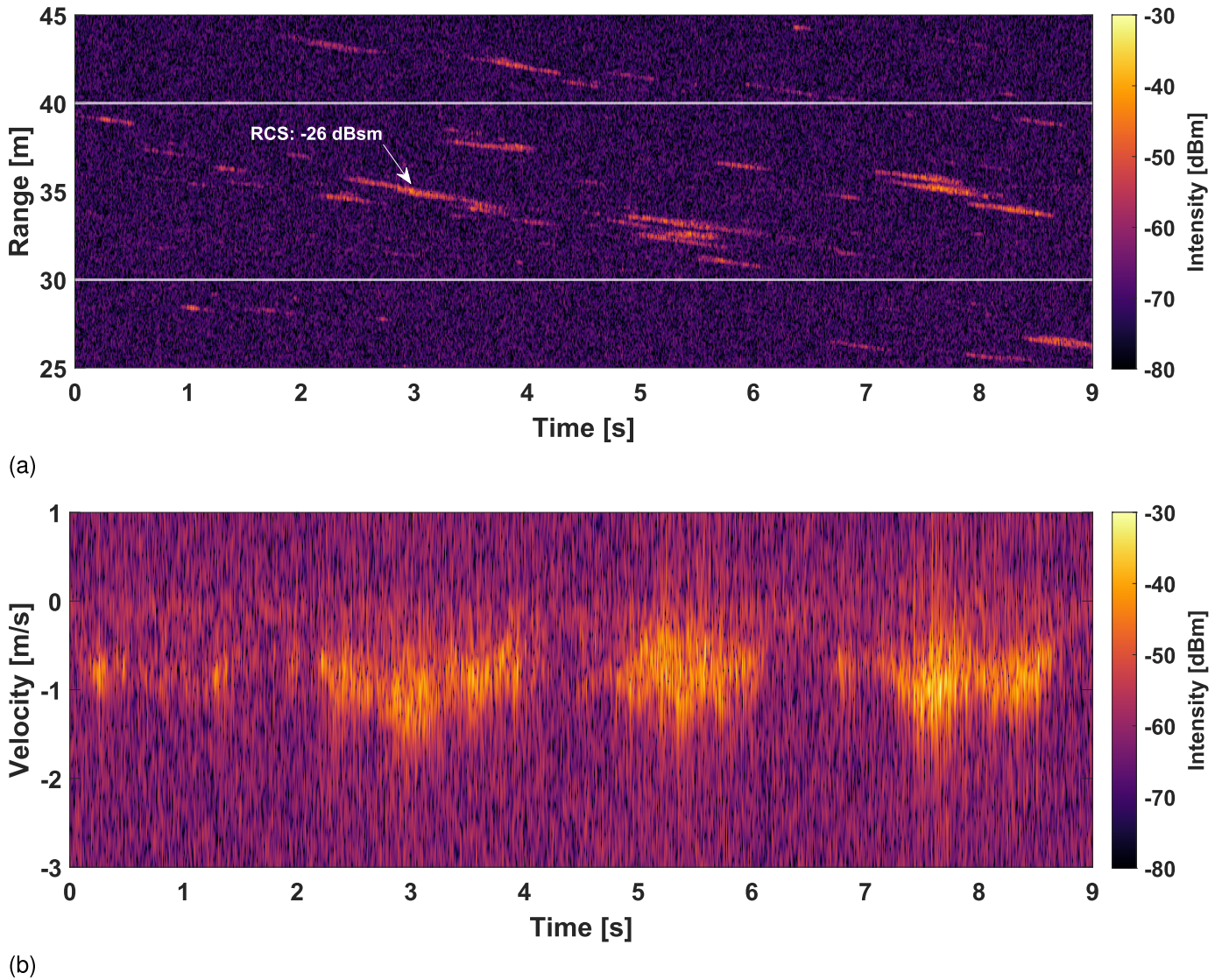
Fig. 14. (a) Range-time-intensity plot and (b) spectrogram of sea clutter observed at 207 GHz at Coniston Water. The spectrogram displays the time-evolving velocity of scatterers for ranges between 30-40 m, as indicated on (a) with horizontal lines.

a few decibels below the ADC limit. The signal peaks other than those at ~11 MHz are due to harmonic distortion in the receiver, where this was reduced in the measurements for the new configuration by changing the second IF amplifier for one with better harmonic performance. The plot also shows the noise floor simulated using Eq. 4:

$$N_{\phi,\text{model}} = A + 10\log_{10}(M)$$
$$+ C \cdot f + D \cdot \exp\left(\frac{-f^2}{K^2}\right)[\text{dB}] \quad (4)$$

Which incorporates the modulation M as defined in Eq. 3, and where the factors A, C, D, and K are empirical model parameters as defined in [66] and were fitted manually. With the original chirp generator, a clear lobing is evident in the reflected phase noise floor which is about 32 dB above the true (thermal) noise floor. This effect would clearly mask weak targets in the same line of sight as the bright target. With the new chirp generator, which has 21.5 dB lower phase noise (Fig. 8), the lobing is still evident but reduced by ~20 dB

as expected and is only about 12 dB above the thermal noise floor.

The phase noise performance could be improved further by upconverting the DDS chirp onto a DRO with ~2x frequency of the Nexyn model (whilst increasing the chirp baseband bandwidth by the same factor), as previously mentioned in Section III. This would reduce the phase noise due to frequency multiplication by a further 6 dB. Electronic DROs with somewhat better phase noise performance could be sourced presently but the gains would be minor. New photonic sources [67] have approximately equivalent phase noise performance but are capable of far greater output frequencies of up to 100 GHz, so potentially only one doubling stage would be needed (for an improvement of ~16 dB), however chirping over the required bandwidth of 1 GHz at baseband would present a greater challenge.

Fig. 13 demonstrates the effect that the phase noise degradation had on the instrument noise floor for Doppler measurements with the old chirp generator configuration,
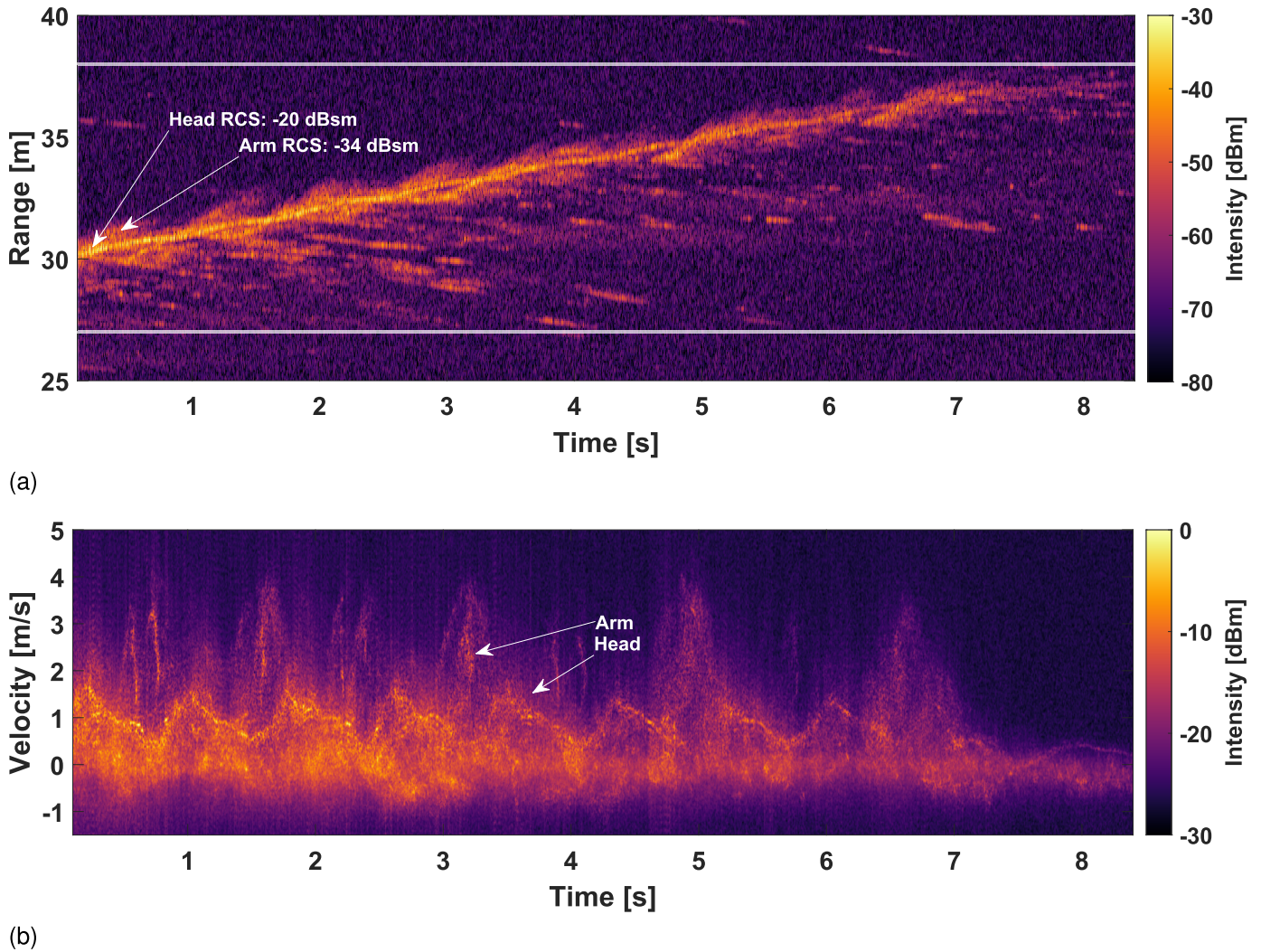
Fig. 15.   (a) Range-time-intensity plot and (b) spectrogram of a man swimming front-crawl observed at 207 GHz at Coniston water. The spectrogram is formed from the ranges indicated in (a) between the horizontal lines.
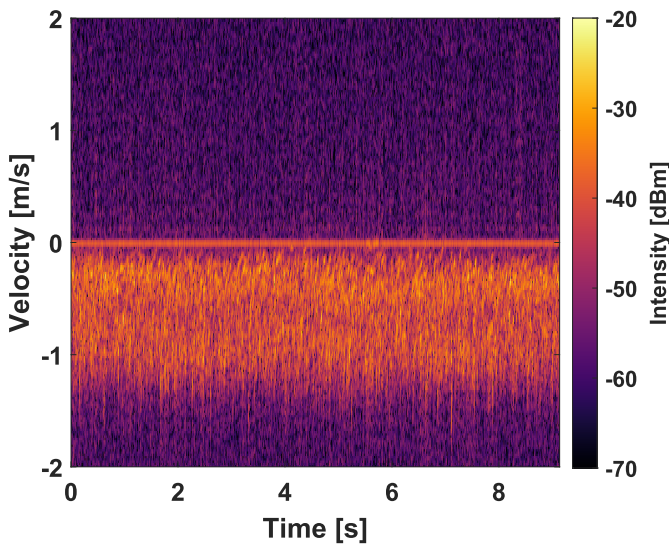

Fig. 16.   Doppler data of moderate rainfall observed pointing towards the horizon.

evident as velocity banding, which clearly would mask moving targets at any velocity in the range bands affected.

VI. INITIAL APPLICATION MEASUREMENTS

In this section we present example data for a selection of potential measurement applications to illustrate the capability of the radar. Data collected by the radar undergoes straight-forward FMCW raw data processing to generate range and Doppler profiles. Some estimates of RCS have been made for features in the plots and indicated where appropriate. These estimates have been calculated by averaging a small number of spot measurements near the indicated point and calibrating this with respect to range using the curve in Fig. 11. These RCS values are only preliminary however, and more definitive values would require a more in-depth analysis to account for the distribution of values and the effects of the antenna beam pattern. This is not within the scope of this paper, but will be performed in future using the characterization results presented.

The real-time radar control code is developed using Lab-Windows/CVI on a quad core PC. Multithreading is used to parallelize processing across the multiple cores, where the control code has separate dedicated threads for data acquisition and data processing. The data capture occurs continuously with simultaneous real-time processing and data saving. Ideally
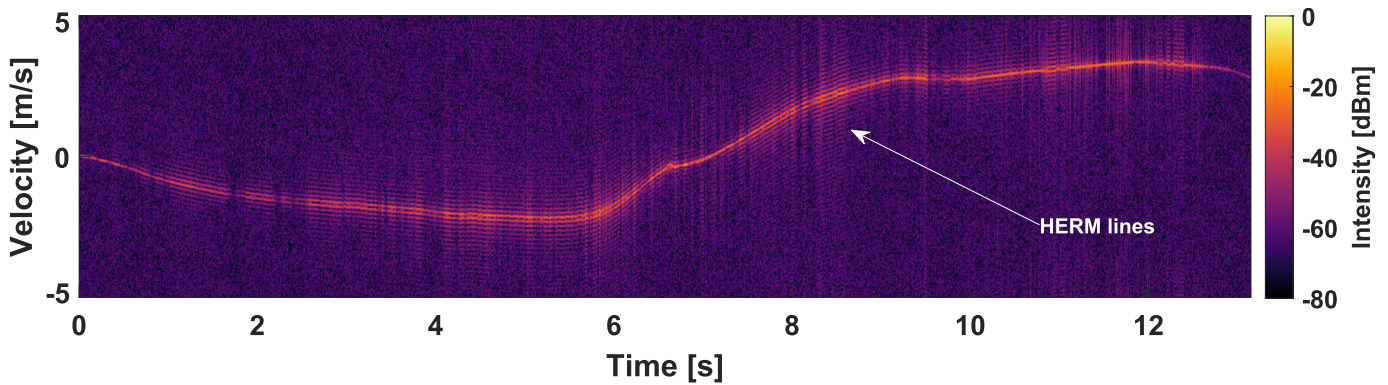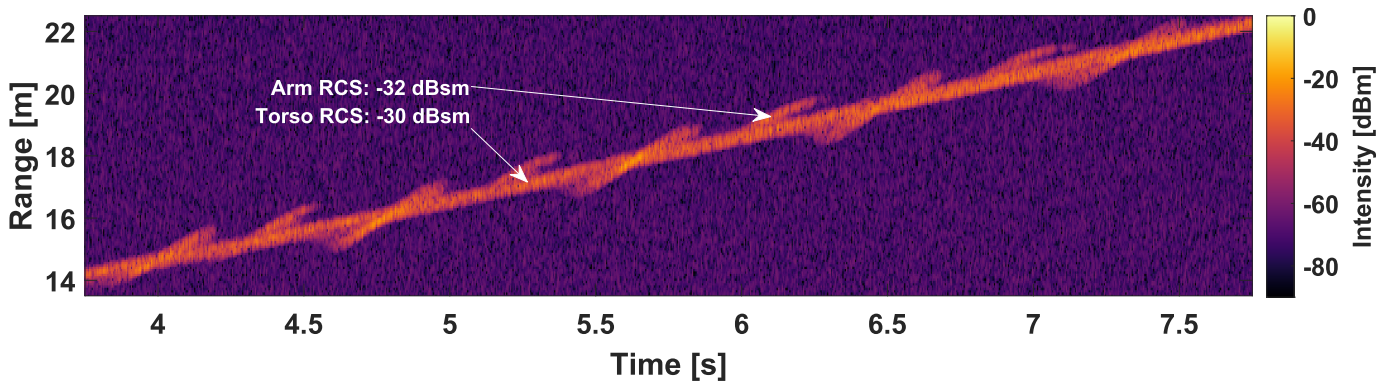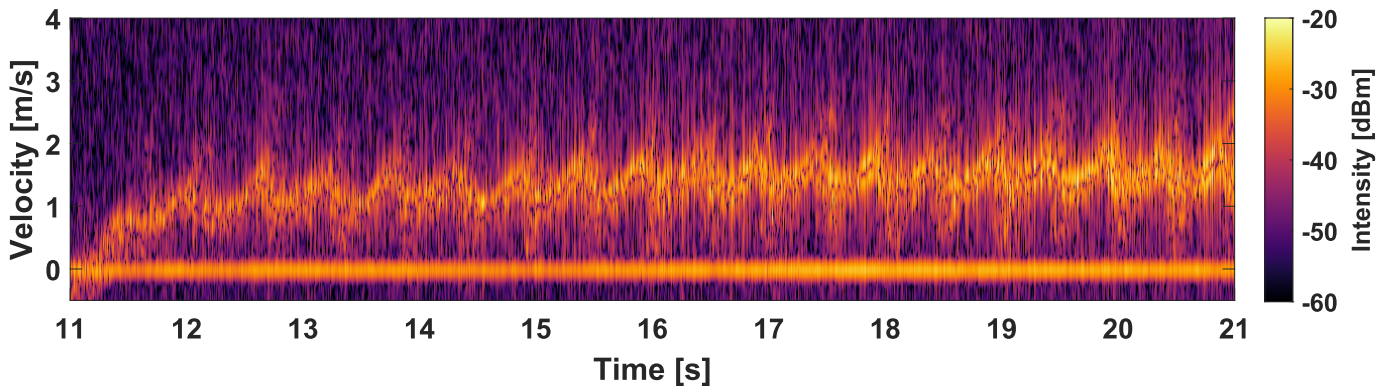
Fig. 17. DJI Phantom 3 Standard UAV spectrogram data.

(a)

(b)

Fig. 18. (a) A range-time-intensity plot of a human running radially away from the radar whilst rotating arms in a windmill-like fashion and (b) a spectrogram of a human running radially away from the radar (different data).

there is no data drop in this whole process, but some intermittent loss has been observed on the scale of 50-100 ms within ∼10 s. The most likely cause is internal memory overload/refresh during continuous data storage. Although the drop is not significant (≤1%), we still intend to improve this at some point in future. The user interface plots both the instantaneous range profile and range-Doppler profile (generated with 64 chirps) in real-time, to provide a reasonably quick plot update rate with good Doppler resolution (231 Hz or 0.16 m s^{-1}).

For more in-depth Doppler analysis, spectrograms are generated offline using the Short Time Fourier Transform (STFT) over longer intervals of time series data. For the results shown in this section, an STFT window length of 512 samples is used, corresponding to a Doppler resolution of 28.9 Hz or 0.02 m s^{-1}. This reveals the temporal variation of target Doppler signatures. A 99% overlap was used during STFT processing to remove any edge effects.

As the ADC sampling rate is 79.55 MHz, the maximum detectable non-aliased IF frequency is 39.78 MHz. Using Eq. 2, this gives the maximum radar instrumented range of 153.5 m, which is ∼2% of 7.7 km, the maximum unambiguous range due to chirp time. The IF chain anti-alias filter strongly suppresses any signal frequency above the cut-off frequency of
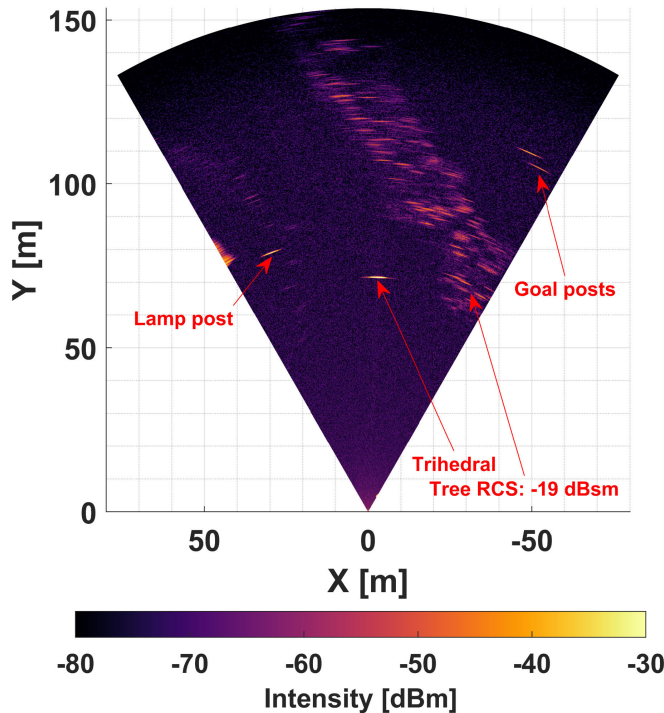
Fig. 19. 60° PPI scan of trihedral and environment at St Andrews Observatory, with aerial image (Google) showing approximate field of regard (note that the trees around the oval running track had been removed prior to the PPI scan).

~32 MHz as shown in Fig. 6. Any aliases above 39.78 MHz folded into the IF frequency range are very unlikely to impact the data since the SNR is likely to be very low.

A. Marine Data

In August 2022 this radar was one of several instruments deployed at Coniston Water in the Lake District, UK, as part of the STREAM project. One of the trial objectives was to measure the NRCS of waves at 207 GHz, where data of the lake surface were gathered in HH and VV polarizations at several different grazing angles and bearings, the latter giving a diversity of wave approach angles with respect to radar line of sight. The conditions during the trial were fair, with low windspeeds of up to 22 km h^{-1}. The wave crests occurring on the lake surface were correspondingly small, up to ~10 cm in height. Some of the data from this trial were used for an analysis comparing the amplitude statistics in HH and VV which is presented in Vattulainen et al. [68].

An example of the RTI plots produced by waves observed during the trial is displayed in Fig. 14, along with the spectrogram from this time interval. The RTI shows waves approaching the shore being observed in the narrow beam of the radar for a grazing angle of 3°. The detected features are very fine due to the range resolution of 7.5 cm, indicating that most of the return from a wave is coming from a very small range extent. The spectrogram is formed from data between 30-40 m, where three main clusters of returns are visible corresponding to the largest returns within this swath. The bulk velocity of each wave is very similar, indicating waves are moving at a constant rate towards the radar at this range.

A significant quantity of marine target data was also collected, including buoys, small boats, and humans swimming, where an example of the latter is shown in Fig. 15. Here the person was moving radially away swimming front-crawl. Several notable features are visible when inspecting the range-time-intensity plot: the bulk diagonal trend shows an average speed of approximately 1 m s^{-1} with a consistent small fluctuation as the swimmer pulls forward and then slows down again in a cycle between each stroke; significant returns are evident from the arms or from spray which creates a broader oscillatory trend; wave crest features are picked up almost exclusively behind the swimmer and moving towards the radar, resulting from the wake behind the swimmer in an otherwise mostly calm surface. In the spectrogram a distinct, sawtooth-like oscillation around a 1 m s^{-1} average is evident from the body as the speed of the swimmer changes through each stroke, as well as lower amplitude returns from the arms moving up to 4 m s^{-1}. Signals from spray and from the wake moving towards the radar are also evident.

B. Rain Clutter

Fig. 16 shows Doppler data of rainfall observed with the radar. For this measurement the radar was looking towards the horizon and as such is measuring the wind vector of the hydrometeors, rather than a measurement towards zenith as would be the case for a conventional precipitation radar. This data was collected at the University of St Andrews Observatory on the 22nd of September 2022, during moderate rainfall. This shows a strong signal return from rain is observable with the radar, where hydrometeors had wind vectors of 0-1 m s^{-1} (radially receding from the radar) at a range of 17 m.

C. Target Data

Some examples of micro-Doppler data are shown in Fig. 17 and Fig. 18. These data were collected at the University of St Andrews Observatory on the 29th of November 2022, during clear, dry weather. For Fig. 17, a DJI Phantom 3 Standard UAV was flown at a height of ∼8-10 m at a distance of ∼32-51 m, where several basic maneuvers were performed on or near radar boresight. Fig. 17 shows the UAV moving away at up to 2.5 m s^{-1}, before turning around and approaching at up to 3.5 m s^{-1}, where distinct helicopter rotation modulation (HERM) lines [69] from the drone rotor blades are evident, where this phenomenon can be used for drone classification [70]. The UAV was clearly detectable at ∼60 m, however the maximum detectable range was not determined.

Fig. 18a shows an RTI of a human running radially away from the radar whilst rotating both arms in a windmill-like fashion. In this figure and in Fig. 15a the very fine range resolution shows the kind of micro-range information obtainable from an RTI plot, this being useful for target classification/discrimination algorithm development. Fig. 18b shows a spectrogram of a human running radially away from the radar, showing a typical signature for this motion.

D. PPI Data

Shown in Fig. 19 is a frame from a PPI scan collected at the University of St Andrews Observatory on the 4th of April 2023 in clear, dry weather. The 60° field of view of the scan covers an area of grass with a stand of trees on an embankment. During the measurement, a trihedral was placed in the scene to provide a strong reflection and check for the presence of harmonics and phase noise artifacts. The figure clearly shows the row of trees along with the line of the embankment diagonally rising from right to left, with a strong reflection coming from the trihedral at (0,70) m, and from a lamppost at (40,80) m.

The example datasets shown above demonstrate the performance of Theseus and highlight the high-fidelity data it is capable of collecting as a result of its high range and Doppler resolutions.

VII. Conclusion

This work presents Theseus, a G-band FMCW Doppler radar designed as a compact instrument for field deployment. Specifically, the radar was designed primarily for the characterization of sea clutter and marine targets as part of an investigation into the use of sub-THz radar as sensors for autonomous marine vessels. More generally, it was also designed for general environmental monitoring and security applications research. The experimental results of various targets shown in Section VI validate the potential for the radar to be used for the stated applications.

The homodyne FMCW Doppler design is fully solid-state with DDS chirp generation resulting in highly linear chirps. The ability to measure weak Doppler targets has been improved over that initially reported by implementing a revised chirp generator design for which the phase noise has been reduced by an average of 21.5 dB. The radar

operates between 200-208 GHz, presently with a 2 GHz chirp bandwidth for a range resolution of 7.5 cm, where these parameters are easily configurable through the control software. Dual in-house designed and fabricated GOLAs with configurable linear polarization are used for transmit and receive, where performance has been characterized at low (200-202 GHz) and high (206-208 GHz) bands, with gains of 37.4 dBi or 37.9 dBi, and one-way beamwidths of 2.13° or 2.05° respectively. In each band, the average transmit powers are +15.3 dBm and +14.4 dBm, with receiver noise figures of 12.1 dB and 14.1 dB respectively. At high band, the noise figure results in a noise floor level of −74 dBm, for a system dynamic range of 84 dB.

The sensitivity of this radar, and hence its maximum operating range, could be improved in future by the addition of a low noise amplifier (LNA) prior to the SHM to reduce the receiver noise figure, and/or by a higher power, wider band W-band power amplifier which would increase the transmit power achieved from the presently drive limited varactor doubler. Nonetheless, in its present configuration, the radar performs according to the design expectations, and demonstrates that the high carrier frequency and wide bandwidth enable the measurement of both micro-Doppler and micro-range information useful in a wide range of applications. Theseus will be invaluable for performing target and clutter phenomenology studies in the presently little explored G-band which potentially offers advantages for high fidelity sensing such as required for vessel or vehicle autonomy.

Acknowledgment

References

[1] J. Nemarich, R. J. Wellman, D. Rocha, and G. B. Wetzel, "A system for measuring near-millimeter wave target signature and propagation characteristics," in *Proc. Electron. Aerosp. Syst. Conv. (EASCON)*, Washington, DC, USA. New York, NY, USA: Institute of Electrical and Electronics Engineers, Nov. 1981, pp. 226–233. [Online]. Available: https://ui.adsabs.harvard.edu/abs/1981easc.conf..226N/abstract

[2] J. Nemarich, R. J. Wellman, and J. Lacombe, "Backscatter and attenuation by falling snow and rain at 96, 140, and 225 GHz," *IEEE Trans. Geosci. Remote Sens.*, vol. 26, no. 3, pp. 319–329, May 1988.

[3] N. C. Currie and C. E. Brown, *Principles and Applications of Millimeter-Wave Radar*, N. C. Currie and C. E. Brown, Eds. Norwood, MA, USA: Artech House, 1987.

[4] R. E. McIntosh, R. M. Narayanan, J. B. Mead, and D. H. Schaubert, "Design and performance of a 215 GHz pulsed radar system," *IEEE Trans. Microw. Theory Techn.*, vol. 36, no. 6, pp. 994–1001, Jun. 1988.

[5] R. M. Narayanan, C. C. Borel, and R. E. McIntosh, "Radar backscatter characteristics of trees at 215 GHz," *IEEE Trans. Geosci. Remote Sens.*, vol. 26, no. 3, pp. 217–228, May 1988.

[6] J. B. Mead, R. E. McIntosh, D. Vandemark, and C. T. Swift, "Remote sensing of clouds and fog with a 1.4-mm radar," *J. Atmos. Ocean. Technol.*, vol. 6, no. 6, pp. 1090–1097, Dec. 1989. [Online]. Available: https://journals.ametsoc.org/view/journals/atot/6/6/1520-0426_1989_006_1090_rsocaf_2_0_co_2.xml, doi: 10.1175/1520-0426(1989)006<1090:RSOCAF>2.0.CO;2.

[7] J. B. Mead and R. E. McIntosh, "A 225 GHz polarimetric radar," *IEEE Trans. Microw. Theory Techn.*, vol. 38, no. 9, pp. 1252–1258, Sep. 1990.

[8] J. B. Mead and R. E. McIntosh, "Polarimetric backscatter measurements of deciduous and coniferous trees at 225 GHz," *IEEE Trans. Geosci. Remote Sens.*, vol. 29, no. 1, pp. 21–28, Jan. 1991.

[9] J. B. Mead, P. M. Langlois, P. S. Chang, and R. E. McIntosh, "Polarimetric scattering from natural surfaces at 225 GHz," *IEEE Trans. Antennas Propag.*, vol. 39, no. 9, pp. 1405–1411, Sep. 1991.

[10] R. W. McMillan, C. W. Trussell, R. A. Bohlander, J. C. Butterworth, and R. E. Forsythe, "An experimental 225 GHz pulsed coherent radar," *IEEE Trans. Microw. Theory Techn.*, vol. 39, no. 3, pp. 555–562, Mar. 1991.

[11] H. Essen et al., "High-bandwidth 220 GHz experimental radar," *Electron. Lett.*, vol. 43, no. 20, pp. 1114–1116, 2007. [Online]. Available: https://digital-library.theiet.org/content/journals/10.1049/el_20071865, doi: 10.1049/el:20071865.

[12] H. Essen et al., "A high performance 220-GHz broadband experimental radar," in *Proc. 33rd Int. Conf. Infr., Millim. THz Waves*, Sep. 2008, pp. 6–7.

[13] H. Essen, A. Wahlen, R. Sommer, M. Schlechtweg, and A. Tessmann, "Development of a 220-GHz experimental radar," in *Proc. German Microw. Conf.*, Mar. 2008, pp. 1–4.

[14] D. T. Petkie, C. Benton, and E. Bryan, "Millimeter wave radar for remote measurement of vital signs," in *Proc. IEEE Radar Conf.*, May 2009, pp. 9–11.

[15] D. T. Petkie et al., "Remote respiration and heart rate monitoring with millimeter-wave/terahertz radars," *Millimetre Wave THz Sensors Technol.*, vol. 7117, Oct. 2008, Art. no. 71170I.

[16] G. P. Timms, "Design and testing of an active 190-GHz millimeter-wave imager," *J. Electron. Imag.*, vol. 19, no. 4, Oct. 2010, Art. no. 043019.

[17] T. Jaeschke, C. Bredendiek, and N. Pohl, "A 240 GHz ultra-wideband FMCW radar system with on-chip antennas for high resolution radar imaging," in *IEEE MTT-S Int. Microw. Symp. Dig.*, Jun. 2013, pp. 1–4.

[18] T. Bryllert, V. Drakinskiy, K. B. Cooper, and J. Stake, "Integrated 200–240-GHz FMCW radar transceiver module," *IEEE Trans. Microw. Theory Techn.*, vol. 61, no. 10, pp. 3808–3815, Oct. 2013.

[19] B. Cheng et al., "Real-time imaging with a 140 GHz inverse synthetic aperture radar," *IEEE Trans. THz Sci. Technol.*, vol. 3, no. 5, pp. 594–605, Sep. 2013.

[20] J. Fritz, L. Scally, A. J. Gasiewski, and K. Zhang, "A sub-terahertz real aperture imaging radar," in *Proc. IEEE Radar Conf.*, May 2014, pp. 1165–1169.

[21] D. A. Robertson, D. G. Macfarlane, and T. Bryllert, "220 GHz wideband 3D imaging radar for concealed object detection technology development and phenomenology studies," *Proc. SPIE*, vol. 9830, May 2016, Art. no. 983009.

[22] J. Grzyb, K. Statnikov, N. Sarmah, B. Heinemann, and U. R. Pfeiffer, "A 210–270-GHz circularly polarized FMCW radar with a Single-Lens-Coupled SiGe HBT chip," *IEEE Trans. THz Sci. Technol.*, vol. 6, no. 6, pp. 771–783, Nov. 2016.

[23] D. Jasteh, E. G. Hoare, M. Cherniakov, and M. Gashinova, "Experimental low-terahertz radar image analysis for automotive terrain sensing," *IEEE Geosci. Remote Sens. Lett.*, vol. 13, no. 4, pp. 490–494, Apr. 2016.

[24] Q. Yang, Y. Qin, K. Zhang, B. Deng, X. Wang, and H. Wang, "Experimental research on vehicle-borne SAR imaging with THz radar," *Microw. Opt. Technol. Lett.*, vol. 59, no. 8, pp. 2048–2052, Aug. 2017.

[25] A. Y. Nashashibi, B. Alazem, and K. Sarabandi, "Fully polarimetric FMCW instrumentation radar at 228 GHz," in *Proc. USNC-URSI Radio Sci. Meeting (Joint With AP-S Symp.)*, Jul. 2017, pp. 35–36. [Online]. Available: http://ieeexplore.ieee.org/document/8074884/

[26] Y. Zhang, Q. Yang, B. Deng, Y. Qin, and H. Wang, "Experimental research on interferometric inverse synthetic aperture radar imaging with multi-channel terahertz radar system," *Sensors*, vol. 19, no. 10, pp. 1–15, 2019.

[27] B. Zeng, M. Liang, C. Zhang, and Y. Zhao, "An experimental 0.2 THz stepped frequency radar system for the target detection," *Proc. SPIE*, vol. 8562, Dec. 2012, Art. no. 85621D.

[28] S. Gu, C. Li, X. Gao, Z. Sun, and G. Fang, "Terahertz aperture synthesized imaging with fan-beam scanning for personnel screening," *IEEE Trans. Microw. Theory Techn.*, vol. 60, no. 12, pp. 3877–3885, Dec. 2012.

[29] Z. Sun, C. Li, S. Gu, and G. Fang, "Fast three-dimensional image reconstruction of targets under the illumination of terahertz Gaussian beams with enhanced phase-shift migration to improve computation efficiency," *IEEE Trans. THz Sci. Technol.*, vol. 4, no. 4, pp. 479–489, Jul. 2014.

[30] M. Y. Liang, C. L. Zhang, R. Zhao, and Y. J. Zhao, "Experimental 0.22 THz stepped frequency radar system for ISAR imaging," *J. Infr., Millim., THz Waves*, vol. 35, no. 9, pp. 780–789, Jun. 2014, doi: 10.1007/s10762-014-0079-7.

[31] M. Moallem and K. Sarabandi, "Polarimetric study of MMW imaging radars for indoor navigation and mapping," *IEEE Trans. Antennas Propag.*, vol. 62, no. 1, pp. 500–504, Jan. 2014.

[32] A. Y. Nashashibi, A. A. Ibrahim, S. Cook, and K. Sarabandi, "Experimental characterization of polarimetric radar backscatter response of distributed targets at high millimeter-wave frequencies," *IEEE Trans. Geosci. Remote Sens.*, vol. 54, no. 2, pp. 1013–1024, Feb. 2016.

[33] H. B. Wallace, "Development of a video SAR for FMV through clouds," *Proc. SPIE*, vol. 9479, May 2015, Art. no. 94790L.

[34] S.-H. Kim, R. Fan, and F. Dominski, "ViSAR: A 235 GHz radar for airborne applications," in *Proc. IEEE Radar Conf. (RadarConf)*, Apr. 2018, pp. 1549–1554.

[35] B. M. Courtier et al., "First observations of G-band radar Doppler spectra," *Geophys. Res. Lett.*, vol. 49, no. 4, Feb. 2022, Art. no. e2021GL096475, doi: 10.1029/2021gl096475.

[36] M. Bian, S. Wang, and W. Hu, "Design and experiment of spaceborne terahertz cloud profiling radar," in *Proc. 42nd Int. Conf. Infr., Millim., THz Waves (IRMMW-THz)*, Aug. 2017, pp. 1–4.

[37] K. B. Cooper et al., "Atmospheric humidity sounding using differential absorption radar near 183 GHz," *IEEE Geosci. Remote Sens. Lett.*, vol. 15, no. 2, pp. 163–167, Feb. 2018.

[38] R. J. Roy, M. Lebsock, L. Millán, and K. B. Cooper, "Validation of a G-Band differential absorption cloud radar for humidity remote sensing," *J. Atmos. Ocean. Technol.*, vol. 37, no. 6, pp. 1085–1102, Jun. 2020.

[39] K. B. Cooper, R. M. Beauchamp, R. J. Roy, L. Millán, M. D. Lebsock, and R. R. Monje, "Cloud dynamics revealed by a G-band humidity-sounding differential absorption radar," in *Proc. IEEE Radar Conf. (RadarConf)*, Sep. 2020, pp. 1–5.

[40] R. J. Roy et al., "First airborne measurements with a G-band differential absorption radar," *IEEE Trans. Geosci. Remote Sens.*, vol. 60, 2022, Art. no. 5108115. [Online]. Available: https://ieeexplore.ieee.org/abstract/document/9653754, doi: 10.1109/TGRS.2021.3134670.

[41] A. V. Muppala, A. Alburadi, A. Y. Nashashibi, H. N. Shaman, and K. Sarabandi, "A 223-GHz FMCW imaging radar with 360° FoV and 0.3° azimuthal resolution enabled by a rotationally stable fan-beam reflector," *IEEE Trans. Geosci. Remote Sens.*, vol. 61, 2023, Art. no. 1000709. [Online]. Available: https://ieeexplore.ieee.org/document/10147337/

[42] O. Levander, "Autonomous ships on the high seas," *IEEE Spectr.*, vol. 54, no. 2, pp. 26–31, Feb. 2017. [Online]. Available: http://ieeexplore.ieee.org/document/7833502/

[43] R. R. Negenborn et al., "Autonomous ships are on the horizon: Here's what we need to know," *Nature*, vol. 615, no. 7950, pp. 30–33, Mar. 2023. [Online]. Available: https://www.nature.com/articles/d41586-023-00557-5

[44] Autonaut Ltd. *Home | Autonaut*. Accessed: Oct. 10, 2023. [Online]. Available: https://www.autonautusv.com/

[45] Saildrone Inc. *Saildrone: Real-time Ocean Data Solutions*. Accessed: Oct. 10, 2023. [Online]. Available: https://www.saildrone.com/

[46] Offshore Sensing AS. *Offshore Sensing-Sailbuoy-Technology*. Accessed: Oct. 10, 2023. [Online]. Available: http://sailbuoy.no/technology

[47] 3Harris Technologies Inc. *C-Worker 5 ASV | L3Harris Fast. Forward.* [Online]. Available: https://www.l3harris.com/all-capabilities/c-worker-5-asv

[48] L. Rosenberg and S. Watts. (Dec. 2021). *Radar Sea Clutter: Modelling and Target Detection*. Inst. Eng. Technol. [Online]. Available: https://digital-library.theiet.org/content/books/ra/sbra530e

[49] C. Waldschmidt, J. Hasch, and W. Menzel, "Automotive radar—From first efforts to future systems," *IEEE J. Microw.*, vol. 1, no. 1, pp. 135–148, Jan. 2021.

[50] S. M. Sabery, A. Bystrov, M. Navarro-Cía, P. Gardner, and M. Gashinova, "Study of low terahertz radar signal backscattering for surface identification," *Sensors*, vol. 21, no. 9, p. 2954, Apr. 2021.

[51] K. D. Ward, R. J. Tough, and S. Watts, *Sea Clutter: Scattering, K Distribution and Radar Performance*, 2nd ed. London, U.K.: Institution of Engineering and Technology, 2006.

[52] A. Raynal and A. Doerry, "Doppler characteristics of sea clutter," Sandia Nat. Laboratories (SNL), Albuquerque, NM, USA, Tech. Rep. SAND2010-3828 and TRN: US201022%%362, Jun. 2010. [Online]. Available: https://www.osti.gov/biblio/992329

[53] F. E. Nathanson, J. P. Reilly, and M. N. Cohen, *Radar Design Principles: Signal Processing and the Environment*, 2nd ed. Rijeka, Croatia: SciTech, 1999.

[54] V. Gregers-Hansen and R. Mital, "An improved empirical model for radar sea clutter reflectivity," *IEEE Trans. Aerosp. Electron. Syst.*, vol. 48, no. 4, pp. 3512–3524, Oct. 2012. [Online]. Available: http://ieeexplore.ieee.org/document/6324732/

[55] H. Essen, H. Fuchs, and A. Pagels, "High resolution millimeterwave SAR for the remote sensing of wave patterns," in *Proc. IEEE Int. Geosci. Remote Sens. Symp. (IGARSS)*, Barcelona, Spain, Jul. 2007, pp. 963–966. [Online]. Available: http://ieeexplore.ieee.org/document/4422959/

[56] A. G. Stove, D. A. Robertson, and D. G. Macfarlane, "Littoral sea clutter returns at 94GHz," in *Proc. Int. Radar Conf.*, Oct. 2014, pp. 1–6.

[57] T. Lamont-Smith, T. Waseda, and C.-K. Rheem, "Measurements of the Doppler spectra of breaking waves," *IET Radar, Sonar Navig.*, vol. 1, no. 2, p. 149, 2007. [Online]. Available: https://digital-library.theiet.org/content/journals/10.1049/iet-rsn_20060109, doi: 10.1049/iet-rsn:20060109.

[58] T. Lamont-Smith, "Doppler spectra of laboratory wind waves at low grazing angle," *Waves Random Media*, vol. 10, no. 1, pp. 33–41, Jan. 2000. [Online]. Available: https://www.tandfonline.com/action/journalInformation?journalCode=twrm20

[59] T. Schlick, M. Gade, H.-H. Essen, K.-W. Gurgel, and P. A. Lange, "W-band radar backscattering at low grazing angles measured in a wave tank at various wind speeds," in *Proc. IEEE Int. Geosci. Remote Sens. Symp.*, Jun. 2002, pp. 1825–1827.

[60] A. B. Vattulainen, S. Rahman, and D. A. Robertson, "G-band FMCW Doppler radar for sea clutter and target characterization," in *Proc. SPIE*, vol. 12108, pp. 292–300, May 2022.

[61] *Radiocommunication Sector of International Telecommunication Union*, document Recommendation ITU-R P.676-10: Attenuation by Atmospheric Gases, 2013.

[62] D. G. Macfarlane, D. A. Robertson, and S. L. Cassidy, "Second generation of AVTIS FMCW millimeter wave radars for mapping volcanic terrain," *Proc. SPIE*, vol. 9829, May 2016, Art. no. 982907, doi: 10.1117/12.2223039.

[63] C. Granet, G. L. James, R. Bolton, and G. Moorey, "A smooth-walled spline-profile horn as an alternative to the corrugated horn for wide band millimeter-wave applications," *IEEE Trans. Antennas Propag.*, vol. 52, no. 3, pp. 848–854, Mar. 2004.

[64] P. F. Goldsmith, *Quasioptical Systems: Gaussian Beam Quasioptical Propagation and Applications*. Hoboken, NJ, USA: Wiley, 1998, doi: 10.1109/9780470546291.

[65] A. Doerry, "Catalog of window taper functions for sidelobe control," Sandia Nat. Laboratories (SNL), Albuquerque, NM, USA, Tech. Rep. SAND2017-4042 and 652561, Apr. 2017. [Online]. Available: https://www.researchgate.net/profile/Armin_Doerry/publication/316281181_Catalog_of_Window_Taper_Functions_for_Sidelobe_Control/links/58f92cb2a6fdccb121c9d54d/Catalog-of-Window-Taper-Functions-for-Sidelobe-Control.pdf and https://www.osti.gov/biblio/1365510

[66] K. B. Cooper, "Modeling broadband phase noise from extended targets in a 170 GHz cloud-imaging radar," in *Proc. Passive Act. Millim.-Wave Imag. XXV*, Jun. 2022, p. 1. https://www.spiedigitallibrary.org/conference-proceedings-of-spie/12111/2621073/Modeling-broadband-phase-noise-from-extended-targets-in-a-170/10.1117/12.2621073.full

[67] E. A. Kittlaus et al., "A low-noise photonic heterodyne synthesizer and its application to millimeter-wave radar," *Nature Commun.*, vol. 12, no. 1, pp. 1–10, Jul. 2021, doi: 10.1038/s41467-021-24637-0.

[68] A. B. Vattulainen, S. Rahman, A. G. Stove, and D. A. Robertson, "Amplitude distribution of low grazing angle G-band littoral sea clutter," in *Proc. IEEE Int. Radar Conf. (RADAR)*, Nov. 2023, pp. 1–6.

[69] D. Blacknell and H. Griffiths, *Radar automatic target recognition (ATR) and Non-Cooperative Target Recognition (NCTR)*. Edison, NJ, USA: IET, 2013.

[70] P. Klaer et al., "An investigation of rotary drone HERM line spectrum under manoeuvering conditions," *Sensors*, vol. 20, no. 20, p. 5940, Oct. 2020. [Online]. Available: https://www.mdpi.com/1424-8220/20/20/5940

Aleksanteri B. Vattulainen (Graduate Student Member, IEEE) received the M.Phys. degree (Hons.) in physics from the University of St Andrews in 2019, the M.S.E.C.E. degree in electrical and computer engineering from Georgia Institute of Technology in 2020, and the Ph.D. degree from the Millimetre Wave Group, University of St Andrews, in Autumn 2020. His Ph.D. concerns the measurement of high frequency sea clutter as part of the STREAM project, including the development of hardware and statistical analysis of data gathered in the field. His research interests include measurements of the radar environment, antenna design, and millimetre-wave radar system design.

Samiur Rahman (Member, IEEE) received the M.Sc. degree in electrical engineering from Blekinge Institute of Technology, Sweden, in 2010, and the Ph.D. degree from University College London (UCL), U.K., in 2015. Since the Ph.D. degree, he has been a Research Fellow with the Millimetre Wave Group, University of St Andrews, U.K. His research interests include radar imaging techniques, radar target classification algorithm development, radar target signature analysis, radar signature modeling, and millimetre-wave radar system design.

Duncan A. Robertson (Member, IEEE) received the B.Sc. degree (Hons.) in physics and electronics and the Ph.D. degree in millimetre wave physics from the University of St Andrews, U.K. For most of his career, he has been with the Millimetre Wave Group, University of St Andrews, working on battlefield systems, passive imaging, electron spin resonance spectroscopy instrumentation, and millimetre wave radar for remote sensing and security applications. His research interests include millimetre-wave radar, radiometry, imaging, electron spin resonance instrumentation, quasi-optics, materials characterization, and antennas.